# High-Throughput Screening Solar-Thermal Conversion Films in a Pseudobinary (Cr, Fe, V)−(Ta, W) System

Qiuwei Xing,[†,‡] Jiang Ma,[§] Cong Wang,[∥] and Yong Zhang*[,†,‡,⊥]

[†]Beijing Advanced Innovation Center for Materials Genome Engineering, Beijing 100083, China

[‡]State Key Laboratory for Advanced Metals and Materials, University of Science and Technology Beijing, Beijing 100083, China

[§]Guangdong Provincial Key Laboratory of Micro/Nano Optomechatronics Engineering, College of Mechatronics and Control Engineering, Shenzhen University, Shenzhen 518060, China

[∥]Center for Condensed Matter and Materials Physics, Beihang University, Beijing 100191, China

[⊥]Beijing Key Laboratory for Magneto-Photo electrical Composite and Interface Science, University of Science and Technology Beijing, Beijing 100083, China

ABSTRACT: The properties and microstructure of (Cr, Fe, V)−(Ta, W) high-entropy films (HEFs) are studied using combinatorial strategies. The compositional library of $(Cr_{0.33}Fe_{0.33}V_{0.33})_x(Ta_{0.5}W_{0.5})_{100-x}$, $(0 < x < 100)$, HEFs are fabricated by cosputtering to discover potential photothermal conversion materials. By verifying points in the compositional library, the structure and property variation according to the atomic content of elements are carefully studied. Results indicate that the films exhibit an amorphous structure when x ranges from 86.9 to 32.5, and high concentrations of Ta and W lead to the formation of a BCC structure in the films. The solar absorptivity of the films peaks at the transitional area from an amorphous to BCC structure. Our research provides an efficient combinatorial technique to discover HEFs with high performance.

KEYWORDS: combinatorial screening, high-entropy film, solar absorptivity
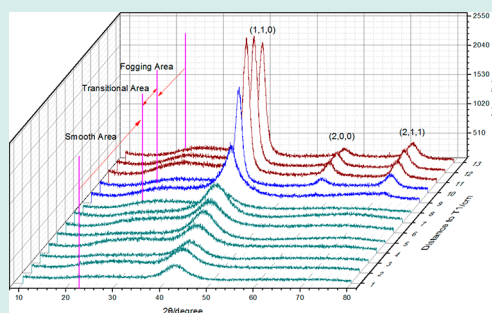
INTRODUCTION

High-entropy alloys (HEAs) were first defined as novel alloys containing five or more equal elements, exhibiting many excellent properties.[1−4] Even though the contents of each element are limited to equal atomic ratio, the number of potential combinations is still large.[5] Moreover, the atomic ratios of elements are not strictly equal in several high-ductility HEAs, such as $Al_{0.3}CoCrFeNi$[6,7] and $Al_{0.5}CrFeNiTi_{0.25}$.[8] The recently reported dual phase HEA of $Fe_{50}Mn_{30}Co_{10}Cr_{10}$,[9] which has improvement in ductility and strength, does not adhere to the equal atomic ratio principle in alloy design. Results indicated that a great number of promising HEAs, especially the multiphase HEAs, exist near the central part of the phase diagram, focusing solely on equal-atomic alloy is insufficient. New materials have traditionally been identified through trial and error, which is not conducive to the development of novel HEAs.

High-throughput fabrication, also called combinatorial fabrication, seeks to identify promising materials by screening many compositions through one experiment. Among combinatorial strategies, combinatorial sputtering is efficient for investigating physical and chemical properties, such as color,[10] corrosion resistance, biocompatibility,[11] antibacterial activity,[12] and glass-forming ability[13,14] in the film. Binary alloy nanometer-scale thin films, such as the TiNi shape memory alloy, can be obtained through cosputtered method[15] or by direct sputtering from the TiNi alloy target.[16] As a special kind of high-entropy materials, high-entropy films (HEFs) can also be fabricated using an HEA target or cosputtered using several pure metal targets. Magnetron sputtering is a vapor deposition process with an extremely high equivalent cooling rate. Precipitations in HEFs are restrained during rapid cooling, and the deposited HEFs exhibit different properties from as-cast HEAs.[17,18] The development of HEFs cannot completely refer to the results of as-cast HEAs and thus require additional experiments to verify their properties. Therefore, applying high-throughput fabrication to HEFs is highly significant.

In this work, we developed novel HEFs consisting of low-activation elements, such as Cr, Fe, V, Ta, and W. Through combinatorial sputtering, compositional libraries of (Cr,Fe,V)−(Ta,W) HEFs were generated on a strip-like silicon wafer. Then, the structure and light absorption properties of the films were investigated to discover their application potential on a photothermal conversion coating. The (Cr,Fe,V)−(Ta,W) HEFs exhibited an amorphous structure when the contents of Ta and W were low, and the structure and surficial qualities each changed as Ta and W increased. Films containing more Ta and W demonstrated better solar
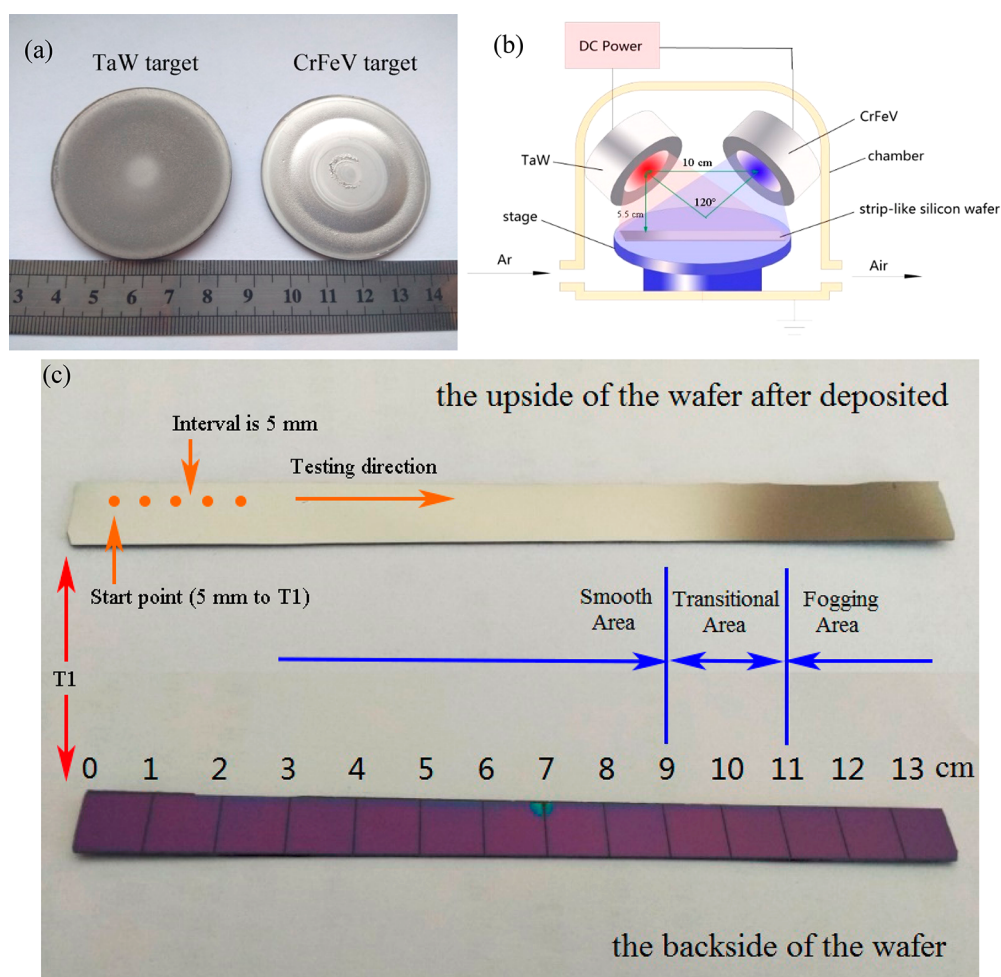
Figure 1. (a) TaW and CrFeV targets used in present work. (b) Magnetron sputtering process to deposit (Cr, Fe, V)−(Ta, W) high-entropy film. (c) Upside of the wafer after deposition (top) and the backside of the wafer was marked before deposition (bottom). Orange points and arrows indicate test points and selected direction on the wafer.

absorptivity, emerging as potential candidates for photo thermal conversion films.

GENERATION OF THE COMPOSITIONAL LIBRARY

First, the (Cr, Fe, V, Ta, W) quinary alloy can be simply considered as a pseudobinary alloy (Cr, Fe, V)-(Ta, W). Refractory elements of tantalum and tungsten are together considered as one pseudocomponent and another containing transition metals (TM) elements in the period table, such as chromium, iron, and vanadium. The elements in each pseudocomponent still have equal atomic ratios to ensure the final alloys have higher entropy than conventional alloys. In this way, the alloy targets of TaW and CrFeV were prepared using an arc-melting method (the purity of metals exceeded 99.9%). The diameter of two targets was 50 mm, and their thickness was 5 mm (Figure 1a).

The distance between the centers of the two targets was 10 cm. The vertical distance from the target center to the substrate was 5.5 cm. The angle of the two-target axis was 120°. The substrate was a strip-like silicon wafer with the size of $1 \times 13 \times 0.1$ cm^3, the backside of which was divided into 13 1×1 cm^2 squares by laser to record the location of each sample (Figure 1b). The upside of the wafer was oxidized to avoid diffusion between the substrate and the film. Subsequently, the wafer was placed at the center of the

stage, the long side of which was parallel to the center-connection line of the two targets. The targets and wafer all maintained a fixed position during the magnetron sputtering process. Although the sputtering yields of Ta and W were lower than those of Cr, Fe, and V, the sputtering power distributed on each component was lower on the ternary alloy target than on the binary alloy target; the sputtering power was 100 W on the CrFeV target and was 80 W on the TaW target under the above conditions. The background pressure was below 1×10^{-3} Pa and the working pressure was set to 0.5 Pa. Both targets were presputtered for 5 min to remove oxide on the surface before being cosputtered for 1 h to form the compositional gradient on the upside of the silicon wafer (Figure 1b). The end of the wafer close to target CrFeV was labeled as terminal 1 (T1), and the end close to target TaW was labeled as terminal 2 (T2).

Samples fabricated using this method offer two advantages: (1) unlike conventional sputtering, the deposited (Cr,Fe,V)-(Ta,W) HEFs possess a large compositional range instead of a certain composition, and required compositions can be easily found on the wafer, and (2) every sample on the wafer is deposited in a single combinatorial sputtering process, thereby minimizing deviation caused by different experimental conditions is minimized.

The thickness of the film was approximately 2 μm and the film transformed from a smooth surface to a fogging surface from T1 to T2. The upside of the wafer could be divided into three different regions after sputtering (Figure 1c) according to the distance to T1. When the distance to T1 was from 0 to 10 cm, the film had a smooth, mirror-like surface, and the region from 11 to 13 cm was fogging. The two regions were separated by a 2 cm-wide nebulous boundary. This broad boundary which was 9−11 cm from T1, represented a transitional area.

■ RESULT AND DISCUSSION

Composition Distribution. As indicated in Figure 1c, the atomic contents of five elements from T1 to T2 on the wafer were tested using energy dispersive spectrometer (EDS) at a interval of 5 mm (Table 1). EDS tests (operated at 15 kV)

Table 1. Atomic Contents of Cr, Fe, V, Ta, and W at 26 Points on the Wafer

| distance to T1 (cm)	Cr (at. %)	Fe (at. %)	V (at. %)	Ta (at. %)	W (at. %)	x
0.5	30	28	29	6	7	87
1	30	28	28	6	8	86
1.5	29	28	28	7	8	85
2	28	27	27	9	9	82
2.5	28	27	26	9	10	81
3	27	26	25	10	12	78
3.5	25	24	24	13	13	74
4	25	23	23	13	15	72
4.5	23	23	22	16	16	68
5	22	21	21	18	18	64
5.5	20	19	18	21	22	57
6	18	17	17	23	24	53
6.5	17	16	16	26	26	48
7	15	14	14	28	29	43
7.5	14	12	12	32	30	38
8	12	11	10	34	33	33
8.5	10	10	9	35	36	29
9	8	8	8	38	38	24
9.5	7	8	6	41	39	21
10	6	6	6	42	40	18
10.5	4	4	5	45	42	13
11	4	5	4	45	42	13
11.5	4	4	4	46	42	12
12	4	4	3	46	43	11
12.5	1	2	3	48	46	6
13	1	2	1	49	47	4

were conducted on wafers in two independent experiments to carry out statistical analysis and avoid occasional one-time incidents. Next, we took the average value as the results and calculated the deviation. Element contents in the same pseudo component were nearly equal. The compositions of the films were essentially followed the molecular formula of $(Cr_{0.33}Fe_{0.33}V_{0.33})_x(Ta_{0.5}W_{0.5})_{100-x}$, $(0 < x < 100)$. Figure 2 displays the atomic content map of five elements based on the distance to T1. At the central part of the wafer, the content distribution was approximately linear according to the distance. The content variation became gentle when the checking points were close to the targets. The contents of Cr and Fe declined abnormally at respective distances of 12.5 and 13 cm, because their sizes were small and hard to detect using EDS. The inset of Figure 2 shows the deviation distribution of EDS data; the
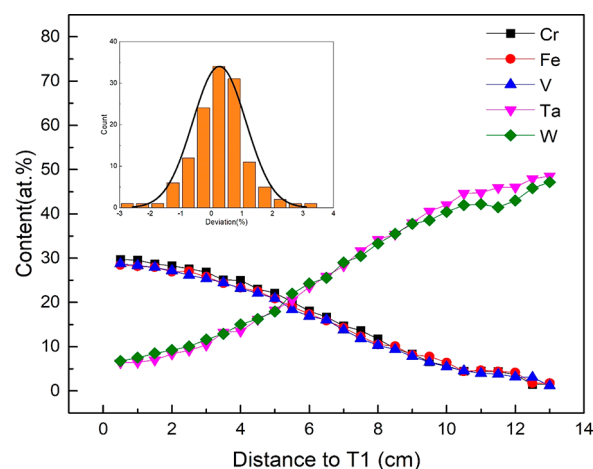
Figure 2. Variations in chemical composition of (Cr, Fe, V)−(Ta, W) high-entropy film at 26 points on the wafer in 0.5 cm intervals; inset illustrates the deviation distribution of EDS data.

confidence interval exceeded 95% when the deviation was less than 2%. The composition of the pseudo components generally followed that of the corresponding targets, and the deposition rates of elements in the same pseudo component were nearly equal.

Structure Analysis. The structure of HEFs varied with element content. The grazing incidence X-ray diffraction measurements (X-ray source was CuKα, the angle of incidence was 1°, and the scanning speed was 4° min^{-1}) were performed on the (Cr, Fe, V)−(Ta, W) film library at room temperature. Along with marks on the backside of the wafer, XRD patterns were checked at 14 points with an interval of 1 cm (corresponding to the test points listed in Table 1; start point was 1 cm to T1). As depicted in Figure 3, the XRD
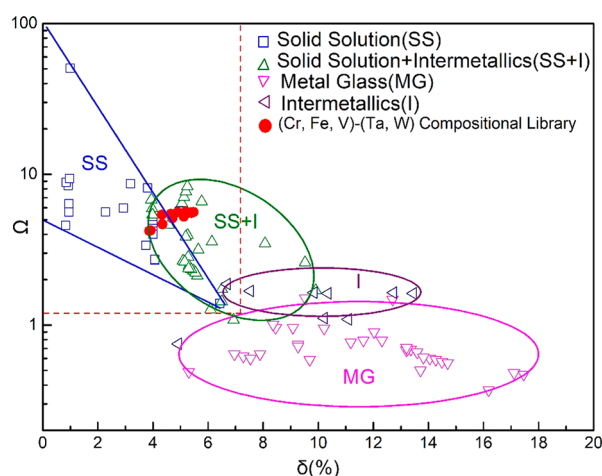
Figure 3. Relationship between parameters Ω and δ for multi-component alloys and (Cr, Fe, V)−(Ta, W) compositional library (region enclosed by red dotted lines is the solid-solution-forming compositional area).

patterns of the smooth area were exhibited in green color, and had only a broad peak; no Bragg peak was observed. The 2 thetas of the broad peak gradually shifted from 41.5° to 39.3° when the position of the sample was farther from the CrFeV target. By contrast, four XRD patterns of the fogging area (in brown) demonstrated three sharp peaks and the films were

found to have a BCC structure. At the transition area (in blue), the broad peak became sharper than the smooth area, and two other minor peaks appeared at 57.1° and 71.0°.

According to Table 1, the $(Cr_{0.33}Fe_{0.33}V_{0.33})_x(Ta_{0.5}W_{0.5})_{100-x}$ HEFs appear to possess an amorphous structure, when $33 < x < 87$. The films were found to have a BCC structure when $4 < x < 13$. Compared with the fogging area, although three peaks were within the same angle, their intensity was weaker. The $(Cr_{0.33}Fe_{0.33}V_{0.33})_x(Ta_{0.5}W_{0.5})_{100-x}$ HEFs contained an amorphous and BCC structure when $18 < x < 24$. As the content of Ta and W increased, the film gradually varied from an amorphous structure to an ordered BCC structure.

The parameter Ω and atomic size differences δ are effective parameters for predicting the phase formation of HEAs, expressed by the equation[19]

$$\Omega = \frac{T_m \Delta S_{mix}}{\Delta H_{mix}} \tag{1}$$

$$\delta = \sqrt{\sum_{i=1}^{n} c_i \left(1 - \frac{r_i}{\Delta r}\right)^2} \tag{2}$$

where the mixing enthalpy $\Delta H_{mix} = \sum_{i=1, i \neq j}^{n} 4 H_{AB}^{mix} c_i c_j$ (H_{AB}^{mix} is the mixing enthalpy for the binary equal atomic AB alloys consisted of the ith and jth components[20]), the mixing entropy $\Delta S_{mix} = -R \sum_{i=1}^{n} (c_i \ln c_j)$; the average atomic radius $\Delta r = \sum_{i=1}^{n} c_i r_i$, c_i, c_j is the mole percent of ith and jth components, r_i is the atomic radius of the ith component; and R is the gas constant ($R = 8.314 \; JK^{-1} \; mol^{-1}$). The melting temperature can be estimated from the ideal mixing rule $T_m = \sum_{i=1}^{n} c_i (T_m)_i$, $(T_m)_i$ is the melting point of the ith component of the alloy.

According to eq 1 and eq 2, the thermal parameters and corresponding phase structure at different wafer positions are listed in Table 2. Reports[19,21−23] have indicated that the solid-

Table 2. Thermal Parameters and Corresponding Phase Structure for (Cr, Fe, V)−(Ta, W) Film at Different Locations on the Wafer

distance to T1 (cm)	ΔS_{mix} (J K^{-1} mol^{-1})	ΔH_{mix} (kJ mol^{-1})	T_m (K)	Ω	δ	phase structure
1	12.01	−4.91	2252	5.51	4.06	MG
2	12.44	−5.43	2304	5.28	4.48	MG
3	12.76	−5.38	2364	5.61	4.71	MG
4	13.07	−5.53	2432	5.75	5.16	MG
5	13.35	−6.22	2561	5.50	5.33	MG
6	13.23	−6.37	2700	5.61	5.56	MG
7	12.88	−6.75	2864	5.46	5.34	MG
8	12.13	−7.09	3002	5.14	5.10	MG
9	11.15	−7.10	3133	4.92	4.59	MG +BCC
10	10.28	−7.17	3214	4.61	4.17	MG +BCC
11	9.40	−7.29	3282	4.23	3.75	BCC
12	9.00	−7.25	3311	4.11	3.55	BCC

solution-forming range of HEAs is $\Omega > \sim 1.1$ and $\delta < \sim 6.6\%$. The mixing enthalpy of solid-solution formation is $\sim 11.6 < \Delta H_{mix} < 3.2 \; kJmol^{-1}$.[22] The thermal parameters listed in Table 2 meet the criteria for solid-solution formation (Figure 3). The δ ranges from 3.53 to 5.45, and the Ω ranges from 4.10 to 5.64, which was in the solid solution forming area (denoted by red dotted line). The XRD patterns in Figure 4 exhibited several

peaks corresponding to a BCC structure when $4 < x < 13$, agreeing well with the phase formation rules of HEAs. Because of the high cooling rate, the $(Cr_{0.33}Fe_{0.33}V_{0.33})_x(Ta_{0.5}W_{0.5})_{100-x}$ HEFs possessed an amorphous structure when $x > 18$. The thermal parameters could not predict phase formation in the HEFs.

The surface topography and cross-section of films were observed using scanning electron microscope (SEM). The amorphous $(Cr_{0.33}Fe_{0.33}V_{0.33})_x(Ta_{0.5}W_{0.5})_{100-x}$ film ($32.5 < x < 86.9$) was smooth, and many cracks were distributed on the surface. When the atomic contents of Ta and W increase to 38 at. %, a few scattered spots appeared on the surface of the film (Figure 5c). With further increasing contents of Ta and W, the spots became larger and denser on the surface of the $Cr_6Fe_6V_6Ta_{42}W_{40}$ film (Figure 5d). At the composition of $Cr_4Fe_5V_4Ta_{45}W_{42}$, the spots adhered to each other completely, but gaps still existed on the surface (Figure 5e). The boundaries of the spots became indistinct, and gaps among the spots disappeared on the surface of the $Cr_4Fe_4V_3Ta_{46}W_{43}$ film (Figure 5f). The SEM cross-sectional image of the $(Cr_{0.33}Fe_{0.33}V_{0.33})_x(Ta_{0.5}W_{0.5})_{100-x}$ film is presented in Figure 6. Tiny columnar structures were distributed in the film when $32.5 < x < 86.9$. Large-grained columnar structures were observed on the cross-section of the film when $x = 24$ and penetrated the whole thickness of the film forming an amorphous structure near the substrate. The films had two clear layers when $4 < x < 13$. A BCC structure layer formed above the amorphous film, and the thickness of the BCC layer was 0.68 μm. The thickness of the film varied from 1.92 to 2.55 nm when x declined from 83 to 18. The deposition rate of the TaW alloy was higher than that of CrFeV.

Optical Properties and Surface Topography. The photothermal conversion coating generally consists of an antireflection layer and absorption layer. Several HEFs possess good thermal stability and mechanical properties at high temperatures, such as NbMoTaW,[24] NbTiAlSi,[25] and NbTiAlSiW[26] HEFs, which are potential candidates for the absorption layer of photothermal conversion coating. However, these HEFs usually have a smooth surface and high surface reflectance with poor solar absorptivity.

The photothermal conversion of the film is generally determined by solar absorptivity and thermal emissivity. For opaque materials, the solar absorptivity α and thermal emissivity ε can be expressed by the equation[27−29]

$$\alpha = \frac{\int_{0.3}^{0.8} I_s(\lambda)(1 - R(\lambda)) \, d\lambda}{\int_{0.3}^{0.8} I_s(\lambda) \, d\lambda} \tag{3}$$

$$\varepsilon = \frac{\int_{0.8}^{1.7} I_b(\lambda)(1 - R(\lambda)) \, d\lambda}{\int_{0.8}^{1.7} I_b(\lambda) \, d\lambda} \tag{4}$$

where $R(\lambda)$ denotes the reflecting ratio of the light with a wavelength of λ, tested experimentally. $I_s(\lambda)$ represents the solar irradiance of light with a wavelength of λ, referring to ASTM G173-03. $I_b(\lambda)$ is the spectral blackbody emissive power of light with a wavelength of λ at room temperature, which can be calculated using the Planck formula.

We applied a UV3100 spectrophotometer equipped with an integrating sphere to measure the reflective spectra $R(\lambda)$ on different areas of the film $(Cr_{0.33}Fe_{0.33}V_{0.33})_x(Ta_{0.5}W_{0.5})_{100-x}$ compositional lab. The internal surface of the integrating
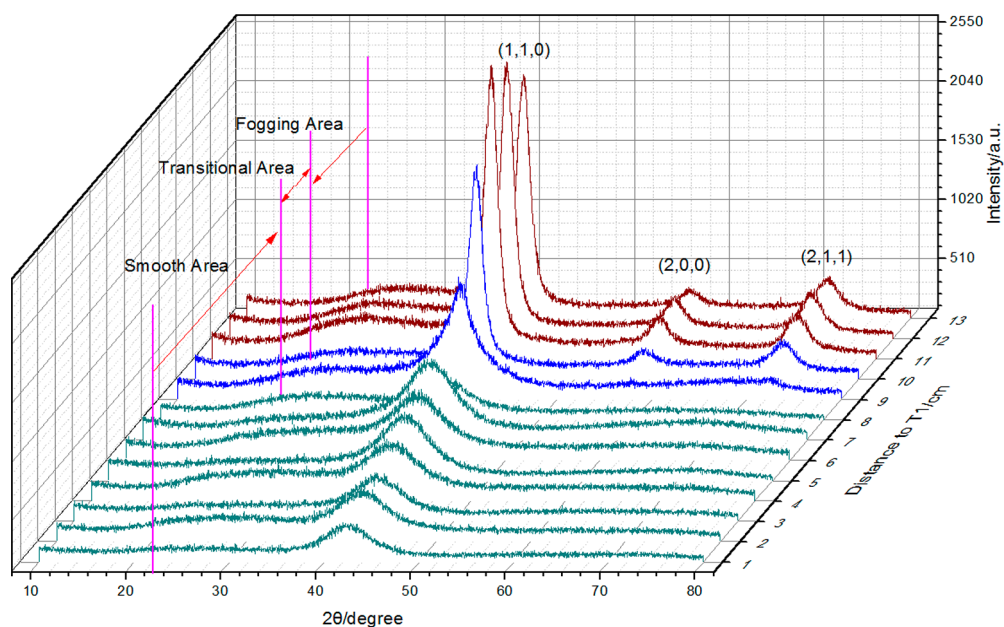
Figure 4. X-ray diffusion patterns at different locations on the wafer (three areas on the substrate are marked by different colors: the smooth area is cyan, transitional area is blue, and fogging area is brown).
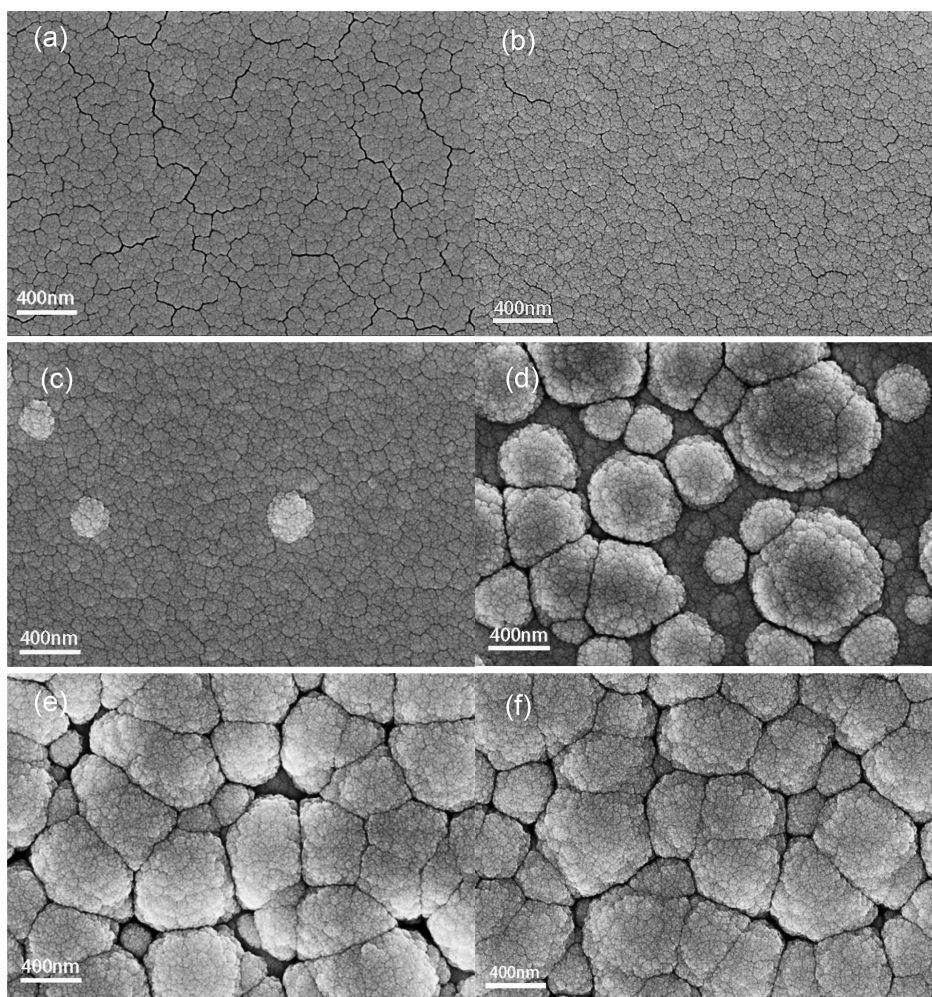
Figure 5. SEM micrograph of the surface of $(Cr, Fe, V)-(Ta, W)$ in various compositions: (a) $Cr_{28.}Fe_{27}V_{27}Ta_9W_9$, (b) $Cr_{12}Fe_{11}V_{10}Ta_{34}W_{33}$, (c) $Cr_8Fe_8V_8Ta_{38}W_{38}$, (d) $Cr_6Fe_6V_6Ta_{42}W_{40}$, (e) $Cr_4Fe_5V_4Ta_{45}W_{42}$, and (f) $Cr_4Fe_4V_3Ta_{46}W_{43}$.
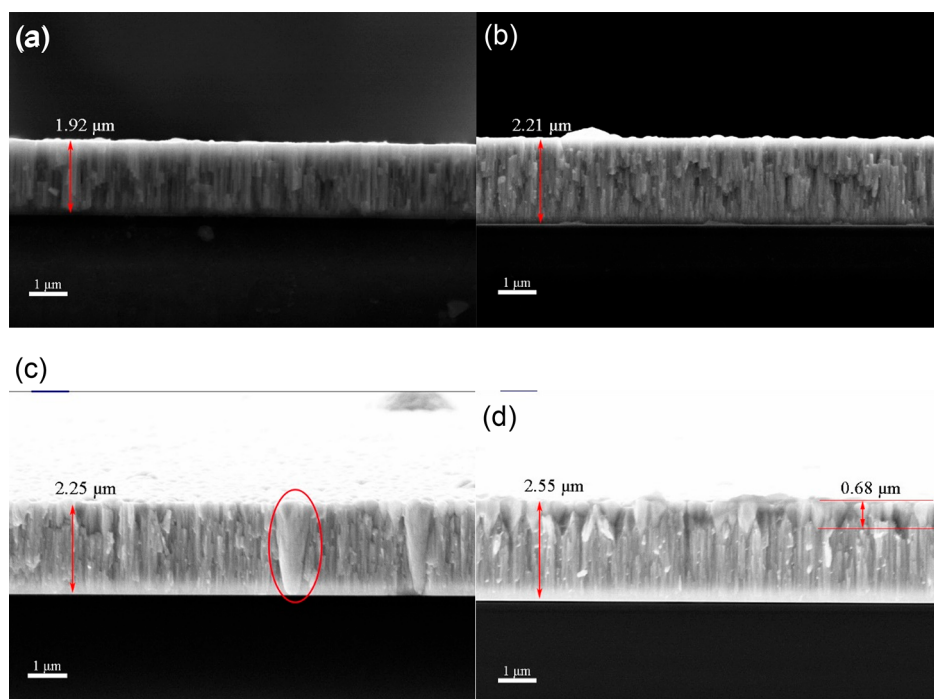
Figure 6. SEM micrograph of cross-section of (Cr, Fe, V)−(Ta, W) in various compositions: (a) $Cr_{28.}Fe_{27}V_{27}Ta_9W_9$, (b) $Cr_{12}Fe_{11}V_{10}Ta_{34}W_{33}$, (c) $Cr_8Fe_8V_8Ta_{38}W_{38}$, and (d) $Cr_6Fe_6V_6Ta_{42}W_{40}$.

sphere was coated with barium sulfate. The wavelength of the incident light ranged from 300 to 1700 nm. According to eqs 3 and 4, the variation curve of solar absorptivity and thermal emissivity are shown in Figure 6. The solar absorptivity was 0.653−0.656 and the thermal emissivity was 0.557−0.582, when the distance to T1 ranged from 2 to 8 cm. The solar absorptivity increased from 0.653 to 0.809 and the thermal emissivity increased from 0.557 to 0.722, corresponding to the distance ranging from 8 to 10 cm. Then, the solar absorptivity declined slightly to 0.789, corresponding to the distance ranging from 10 to 12 cm. The solar absorptivity and the thermal emissivity of the films at transitional area were superior to samples in other positions.

Atomic force microscopy was conducted under ambient temperature to characterize the roughness variation of the surface; the Figure 8 shows the three-dimensional morphologies of four typical surfaces of the film. The film at the smooth area on the wafer had a flat surface topography (Figure 8a) with roughness ranging from 3.39 to 4.02 nm. The roughness increased sharply at the transitional area with spots appearing on the surface of the film (Figure 8b). The maximum value of the roughness measured at the distance of 10 cm was 61.95 nm, exhibiting a composition of $Cr_6Fe_6V_6Ta_{42}W_{40}$ (Figure 8c). According to Figure 8, when x ranged from 13 to 4, sunken areas on the surface were gradually covered by extended white spots, and the surface roughness of the film fell slightly from 61.95 to 40.18 nm, but was still much rougher than films at the distance from 1 to 8 cm (Figure 8d). These results aligned well with the SEM images. The roughness of the film is also displayed in Figure 7.

When expanding the Boltzmann's entropic equation to the equal atomic alloy system, the configurational entropy per mole can be expressed as[30]

$$S_{conf} = R \ln N \tag{4a}$$

where R is the gas content and N is the number of components. In configurational entropy, alloys can be divided into three categories: low-entropy alloys (LEAs), medium-entropy alloys (MEAs), and high-entropy alloys (HEAs). LEAs are unequal atomic binary alloys and pure metals. The major component number of these alloys is less than 2, and their configurational entropy S_{conf} is less than $0.69R$ ($S_{conf} < R \log 2$, according to eq 4). Another type of alloys consists of at least five elements, known as HEAs. For equal atomic HEAs, the configurational entropy S_{conf} is not less than $1.61R$ ($S_{conf} \geq R \log 5$). Similarly, alloys are defined as MEAs when $0.69R \leq S_{conf} < 1.61R$ ($R \log 2 \leq S_{conf} < R \log 5$). Although several HEAs reportedly possess excellent properties, those with higher configurational entropy do not always exhibit better properties than lower ones. In fact, most well-known alloys, such as austenitic stainless steel (1Cr18Ni9Ti) and BMGs, are MEAs. The inset of Figure 7b illustrates the variation of mixing entropy of compositional gradient films. The mixing entropy ΔS_{mix} reached $1.61R$ when the concentrations of the five components were equal. The concentration of the elements could not be exactly equal in the experiment. The mixing entropy of compositional gradient films did not strictly agree with the HEAs criterion but is still much higher than in binary alloy films.

Unlike HEAs, the design strategy of MEAs does not strictly follow the "equal atomic rules", and there are billions of possible element combinations; this fact greatly increases the difficulty in identifying potential alloys with optimal properties using "try and error" method. Therefore, the combinatorial strategy is necessary to solve this problem.
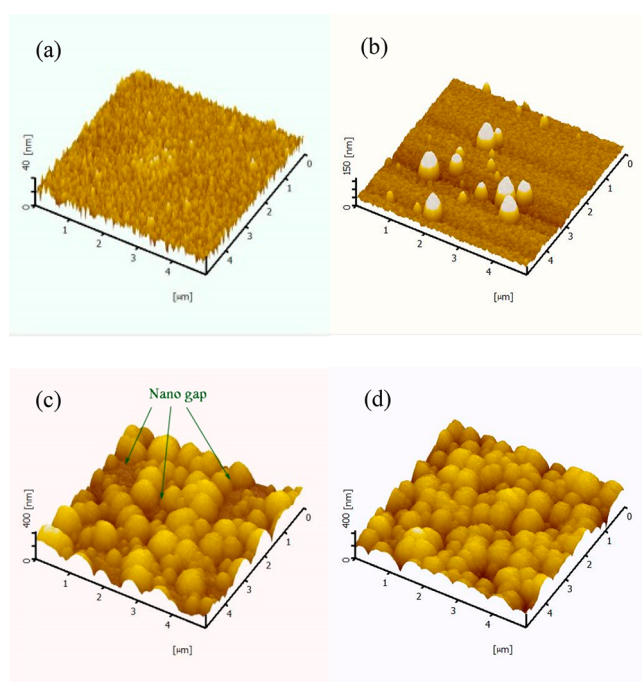
Solar absorption and thermal emissivity were affected by the columnar structure in the film according to the cross-section image. In the smooth area, the film was full of tiny columnar structures, leading to low solar absorption and thermal emissivity. In the transition area, the BCC structure phase
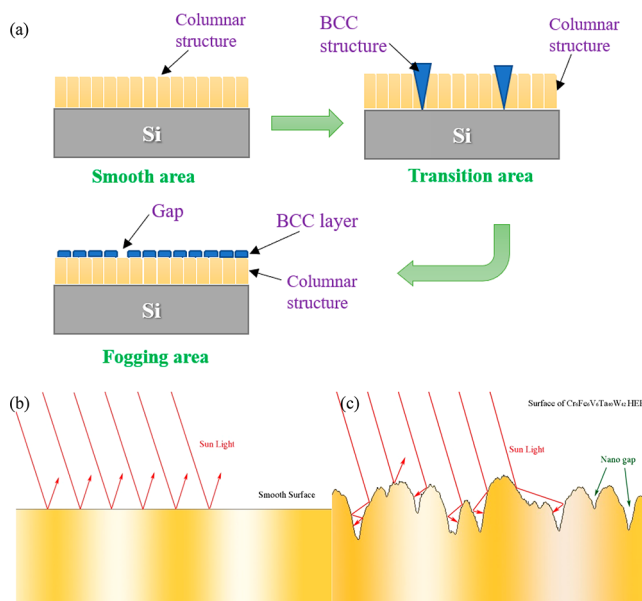
F
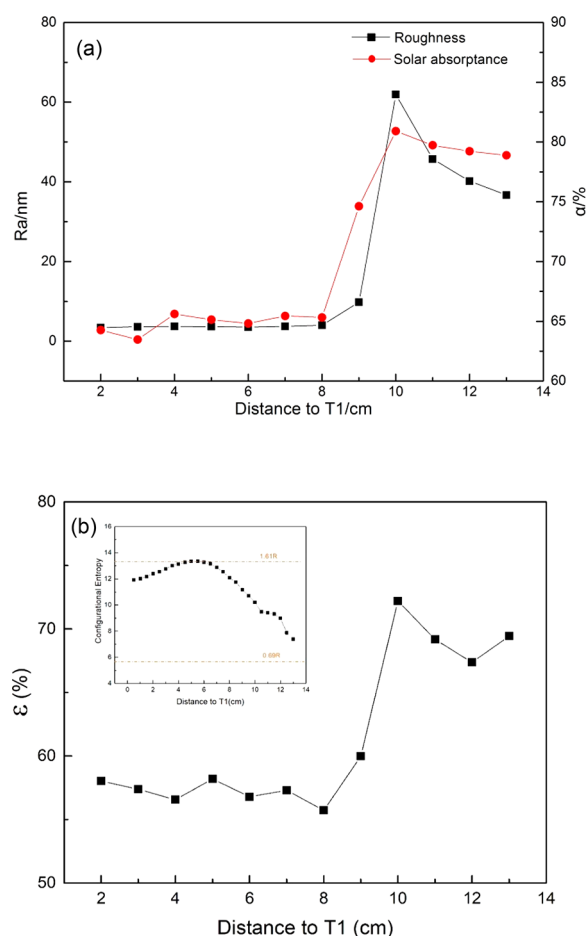
Figure 7. (a) Variations in the toughness and light absorption ratio of the $(Cr_{0.33}Fe_{0.33}V_{0.33})_x(Ta_{0.5}W_{0.5})_{100-x}$ high entropy films according to composition. (b) Variations in toughness and light absorption ratio of $(Cr_{0.33}Fe_{0.33}V_{0.33})_x(Ta_{0.5}W_{0.5})_{100-x}$ high-entropy films. Inset illustrates variations in the mixing entropy of the film according to composition.

Figure 8. Three-dimensional morphologies of four typical surfaces of (Cr, Fe, V)−(Ta, W) high-entropy films (a) $Cr_{12}Fe_{11}V_{10}Ta_{34}W_{33}$, (b) $Cr_8Fe_8V_8Ta_{38}W_{38}$, (c) $Cr_6Fe_6V_6Ta_{42}W_{40}$, and (d) $Cr_4Fe_5V_4Ta_{45}W_{42}$.

Figure 9. (a) Structure variation in (Cr, Fe, V)−(Ta, W) high-entropy films. (b) Schematic illustration of absorbing sunlight for smooth surface. (c) Schematic illustration of absorbing sunlight for surface of $Cr_6Fe_6V_6Ta_{40}W_{42}$ high-entropy film.

embedded into the tiny columnar structures and the film is the mixture of large and tiny columnar structures. The roughness of the film increased to maximum. In the fogging area, the BCC structure separated from tiny columnar structures and gradually covered the surface of the film with increasing contents of Ta and W. The roughness of the film was slightly reduced (Figure 9a). According to Figure 7, the solar absorptivity was positively associated with the surface roughness of the film. When shining on the smooth surface, sunlight was reflected directly away from the film, and the solar absorptivity of the film was low (Figure 9b). However, the roughness increased to 61.95 nm and gaps in uncovered areas were reduced to a nanoscale on the surface of $Cr_6Fe_6V_6Ta_{42}W_{40}$ HEF (Figure 8c). The optical paths were trapped in the gaps between the spots in the reflection process (Figure 9c); therefore, the solar absorptivity of the film was enhanced. With further expansion of the spots, some gaps were filled (Figure 8d), and the solar absorptivity of the film declined accordingly.[31] As demonstrated in Figure 4 and Figure 5, the light-trapped structure on the surface of $(Cr_{0.33}Fe_{0.33}V_{0.33})_x(Ta_{0.5}W_{0.5})_{100-x}$ HEF was caused by nanocrystallization with proper composition. Thus, to fix HEF composition, many samples must be fabricated and their phase structures must be characterized. The combinatorial method is

efficient for screening vast compositional ranges and facilitates the development of high-performance HEFs.

CONCLUSION

Novel multicomponent films of $(Cr_{0.33}Fe_{0.33}V_{0.33})_x(Ta_{0.5}W_{0.5})_{100-x}$ were combinatorially fabricated as a gradient-composition film on a stripe like wafer. By checking the points in the compositional library, the solar absorptivity and structure of the film were investigated. The

G

$(Cr_{0.33}Fe_{0.33}V_{0.33})_x(Ta_{0.5}W_{0.5})_{100-x}$ films retained an amorphous structure when $33 < x < 87$, and a BCC structure appeared when $x < 24$. Variations in solar absorptivity were correlated with the surface roughness of the $(Cr_{0.33}Fe_{0.33}V_{0.33})_x(Ta_{0.5}W_{0.5})_{100-x}$ film. The solar absorptivity reached 81.94% with the composition of $Cr_6Fe_6V_6Ta_{42}W_{40}$, which is the highest value among the verified compositions. These results suggest that combinatorial strategies are an effective approach to obtain the optimal properties from a wide composition range.

■ AUTHOR INFORMATION

Corresponding Author

*E-mail: drzhangy@ustb.edu.cn. Tel: 010-62233073. Fax: 010-62233447.

ORCID ◉

Qiuwei Xing: 0000-0002-8173-8554
Cong Wang: 0000-0002-4100-4222
Yong Zhang: 0000-0002-6355-9923

Notes

The authors declare no competing financial interest.

■ ACKNOWLEDGMENTS

■ REFERENCES

(1) Zhang, Y.; Zuo, T. T.; Tang, Z.; Gao, M. C.; Dahmen, K. A.; Liaw, P. K.; Lu, Z. P. Microstructures and properties of high-entropy alloys. *Prog. Mater. Sci.* **2014**, *61*, 1−93.

(2) Xia, S.; Gao, M. C.; Yang, T.; Liaw, P. K.; Zhang, Y. Phase stability and microstructures of high entropy alloys ion irradiated to high doses. *J. Nucl. Mater.* **2016**, *480*, 100−108.

(3) Zhang, W.; Liaw, P. K.; Zhang, Y. Science and technology in high-entropy alloys. *SCIENCE CHINA Materials* **2018**, *61*, 2−22.

(4) Gludovatz, B.; Hohenwarter, A.; Catoor, D.; Chang, E. H.; George, E. P.; Ritchie, R. O. A fracture-resistant high-entropy alloy for cryogenic applications. *Science* **2014**, *345*, 1153−1158.

(5) Yeh, J. W.; Chen, S. K.; Lin, S. J.; Gan, J. Y.; Chin, T. S.; Shun, T. T.; Tsau, C. H.; Chang, S. Y. Nanostructured High-Entropy Alloys with Multiple Principal Elements: Novel Alloy Design Concepts and Outcomes. *Adv. Eng. Mater.* **2004**, *6*, 299−303.

(6) Li, D.; Zhang, Y. The ultrahigh charpy impact toughness of forged AlxCoCrFeNi high entropy alloys at room and cryogenic temperatures. *Intermetallics* **2016**, *70*, 24−28.

(7) Li, D.; Li, C.; Feng, T.; Zhang, Y.; Sha, G.; Lewandowski, J. J.; Liaw, P. K.; Zhang, Y. High-entropy Al0.3CoCrFeNi alloy fibers with high tensile strength and ductility at ambient and cryogenic temperatures. *Acta Mater.* **2017**, *123*, 285−294.

(8) Liu, S.; Gao, M. C.; Liaw, P. K.; Zhang, Y. Microstructures and mechanical properties of AlxCrFeNiTi0.25 alloys. *J. Alloys Compd.* **2015**, *619*, 610−615.

(9) Li, Z.; Pradeep, K. G.; Deng, Y.; Raabe, D.; Tasan, C. C. Metastable high-entropy dual-phase alloys overcome the strength-ductility trade-off. *Nature* **2016**, *534*, 227−230.

(10) Liu, J.; Liu, Y.; Gong, P.; Li, Y.; Moore, K. M.; Scanley, E.; Walker, F.; Broadbridge, C. C.; Schroers, J. Combinatorial exploration of color in gold-based alloys. *Gold Bull.* **2015**, *48*, 111−118.

(11) Li, J.; Gittleson, F. S.; Liu, Y.; Liu, J.; Loye, A. M.; McMillon-Brown, L.; Kyriakides, T. R.; Schroers, J.; Taylor, A. D. Exploring a wider range of Mg-Ca-Zn metallic glass as biocompatible alloys using combinatorial sputtering. *Chem. Commun.* **2017**, *53*, 8288.

(12) Liu, Y.; Padmanabhan, J.; Cheung, B.; Liu, J.; Chen, Z.; Scanley, B. E.; Wesolowski, D.; Pressley, M.; Broadbridge, C. C.; Altman, S.; Schwarz, U. D.; Kyriakides, T. R.; Schroers, J. Combinatorial development of antibacterial Zr-Cu-Al-Ag thin film metallic glasses. *Sci. Rep.* **2016**, *6*, 26950.

(13) Li, Y.; Guo, Q.; Kalb, J. A.; Thompson, C. V. Matching Glass-Forming Ability with the Density of the Amorphous Phase. *Science* **2008**, *322*, 1816.

(14) Ding, S.; Liu, Y.; Li, Y.; Liu, Z.; Sohn, S.; Walker, F. J.; Schroers, J. Combinatorial development of bulk metallic glasses. *Nat. Mater.* **2014**, *13*, 494−500.

(15) Hou, H.; Hamilton, R. F.; Horn, M. W.; Jin, Y. NiTi thin films prepared by biased target ion beam deposition co-sputtering from elemental Ni and Ti targets. *Thin Solid Films* **2014**, *570*, 1−6.

(16) Kauffmann-Weiss, S.; Hahn, S.; Weigelt, C.; Schultz, L.; Wagner, M. F. X.; Fähler, S. Growth, microstructure and thermal transformation behaviour of epitaxial Ni-Ti films. *Acta Mater.* **2017**, *132*, 255−263.

(17) An, Z.; Jia, H.; Wu, Y.; Rack, P. D.; Patchen, A. D.; Liu, Y.; Ren, Y.; Li, N.; Liaw, P. K. Solid Solution CrCoCuFeNi High Entropy Alloy Thin Films Synthesized by Sputter Deposition. *Mater. Res. Lett.* **2015**, *3*, 203−209.

(18) Zhang, Y.; Yan, X.; Liao, W.; Zhao, K. Effects of Nitrogen Content on the Structure and Mechanical Properties of (Al0.5CrFeNiTi0.25)Nx High-Entropy Films by Reactive Sputtering. *Entropy* **2018**, *20*, 624.

(19) Yang, X.; Zhang, Y. Prediction of high-entropy stabilized solid-solution in multi-component alloys. *Mater. Chem. Phys.* **2012**, *132*, 233−238.

(20) Takeuchi, A.; Inoue, A. Classification of Bulk Metallic Glasses by Atomic Size Difference, Heat of Mixing and Period of Constituent Elements and Its Application to Characterization of the Main Alloying Element. *Mater. Trans.* **2005**, *46*, 2817−2829.

(21) Xing, Q.; Zhang, Y. Amorphous phase formation rules in high-entropy alloys. *Chin. Phys. B* **2017**, *26*, 018104.

(22) Guo, S.; Hu, Q.; Ng, C.; Liu, C. T. More than entropy in high-entropy alloys: Forming solid solutions or amorphous phase. *Intermetallics* **2013**, *41*, 96−103.

(23) Ruiz-Yi, B.; Bunn, J. K.; Stasak, D.; Mehta, A.; Besser, M.; Kramer, M. J.; Takeuchi, I.; Hattrick-Simpers, J. The Different Roles of Entropy and Solubility in High Entropy Alloy Stability. *ACS Comb. Sci.* **2016**, *18*, 596−603.

(24) Zou, Y.; Ma, H.; Spolenak, R. Ultrastrong ductile and stable high-entropy alloys at small scales. *Nat. Commun.* **2015**, *6*, 7748.

(25) Sheng, W.; Yang, X.; Zhu, J.; Wang, C.; Zhang, Y. Amorphous phase stability of NbTiAlSiNx high-entropy films. *Rare Met.* **2018**, *37*, 682.

(26) Sheng, W.; Yang, X.; Wang, C.; Zhang, Y. Nano-Crystallization of High-Entropy Amorphous NbTiAlSiWxNy Films Prepared by Magnetron Sputtering. *Entropy* **2016**, *18*, 226.

(27) Boström, T. K.; Wäckelgård, E.; Westin, G. Anti-reflection coatings for solution-chemically derived nickel-alumina solar absorbers. *Sol. Energy Mater. Sol. Cells* **2004**, *84*, 183−191.

(28) Liu, H. D.; Wan, Q.; Xu, Y. R.; Luo, C.; Chen, Y. M.; Fu, D. J.; Ren, F.; Luo, G.; Cheng, X. D.; Hu, X. J.; Yang, B. Long-term thermal stability of CrAlO-based solar selective absorbing coating in elevated temperature air. *Sol. Energy Mater. Sol. Cells* **2015**, *134*, 261−267.

(29) Ning, Y.; Wang, W.; Wang, L.; Sun, Y.; Song, P.; Man, H.; Zhang, Y.; Dai, B.; Zhang, J.; Wang, C.; Zhang, Y.; Zhao, S.; Tomasella, E.; Bousquet, A.; Cellier, J. Optical simulation and preparation of novel Mo/ZrSiN/ZrSiON/SiO2 solar selective absorbing coating. *Sol. Energy Mater. Sol. Cells* **2017**, *167*, 178−183.

(30) Zhang, Y.; Zhou, Y. J. Solid Solution Formation Criteria for High Entropy Alloys. *Mater. Sci. Forum* **2007**, *561−565*, 1337−1339.

(31) Moon, J.; Lu, D.; VanSaders, B.; Kim, T. K.; Kong, S. D.; Jin, S.; Chen, R.; Liu, Z. High performance multi-scaled nanostructured

spectrally selective coating for concentrating solar power. *Nano Energy* **2014**, *8*, 238−246.